

# Assessing exchange-correlation functional performance for structure and property predictions of oxyfluoride compounds from first principles

Nenian Charles<sup>1,2</sup> and James M. Rondinelli<sup>2,\*</sup>

<sup>1</sup>*Department of Materials Science and Engineering, Drexel University, Philadelphia, Pennsylvania 19104, USA*

<sup>2</sup>*Department of Materials Science and Engineering, Northwestern University, Evanston, Illinois 60208, USA*

(Received 15 August 2016; revised manuscript received 20 October 2016; published 16 November 2016)

Motivated by the resurgence of electronic and optical property design in ordered fluoride and oxyfluoride compounds, we present a density functional theory (DFT) study of 19 materials with structures, ranging from simple to complex, and variable oxygen-to-fluorine ratios. We focus on understanding the accuracy of the exchange-correlation potentials ( $V_{xc}$ ) to DFT for the prediction of structural, electronic, and lattice dynamical properties at four different levels of theory, i.e., the local density approximation (LDA), generalized gradient approximation (GGA), metaGGA, and hybrid functional level which includes fractions of exact exchange. We investigate in detail the metaGGA functionals MS2 [Sun *et al.*, *Phys. Rev. Lett.* **111**, 106401 (2013)] and SCAN [Sun *et al.*, *Phys. Rev. Lett.* **115**, 036402 (2015)], and show that although the metaGGAs show improvements over the LDA and GGA functionals in describing the electronic structure and phonon frequencies, the static structural properties of fluorides and oxyfluorides are often more accurately predicted by the GGA-level Perdew-Burke-Ernzerhof functional for solids, PBEsol. Results from LDA calculations are unsatisfactory for any compound, regardless of oxygen concentration. The PBEsol and Heyd-Scuseria-Ernzerhof (HSE06) functionals give good performance in all-oxide or all-fluoride compounds. For the oxyfluorides, PBEsol is consistently more accurate for structural properties across all oxygen concentrations; however, we stress the need for detailed property assessment with various functionals for oxyfluorides with variable composition. The “best” functional is anticipated to be more strongly dependent on the property of interest. Our study provides useful insights in selecting an  $V_{xc}$  that achieves optimal performance compromises, enabling more accurate predictive design of functional fluoride-based materials with density functional theory.

DOI: [10.1103/PhysRevB.94.174108](https://doi.org/10.1103/PhysRevB.94.174108)

## I. INTRODUCTION

Materials researchers are increasingly utilizing first-principles simulations to elucidate underlying physical principles, guide compound design, and accelerate discovery. In particular, density functional theory (DFT) calculations have proved the method of choice for many researchers owing to its speed and scalability compared to traditional many-body approaches [1,2]. DFT benefits from treating a fictitious, Kohn-Sham system of noninteracting electrons to obtain the interacting electron density. Although the formalism is exact, there remains no complete and tractable description of the exact exchange-correlation (XC) potential ( $V_{xc}$ ) and thus it must be approximated in any practical calculation [3]. As a consequence, the accuracy of these first-principles simulations depends intimately on the suitability of the XC approximation for handling the chemical system and physical property of interest. Owing to the diversity of bonding interactions present in structurally complex and chemically diverse compounds, various  $V_{xc}$  approximations are routinely benchmarked against experimental values of representative compounds in different chemical families to assess and calibrate accuracy [4].

In this light, the burgeoning field of anion engineering in crystalline materials [5], which aims to tune physical properties through the incorporation of multiple-anion species of different size, electronegativity, and charge into the same anionic groups comprising the solid, may present considerable challenges to the predictive capabilities of DFT. Multianion

engineering expands the current set of design strategies for the discovery of functional materials. Oxynitride compounds display interesting dielectric, magnetoelectric, and photocatalytic properties [6–8]. In addition, superconductivity and ferromagnetic behavior have been reported in novel multianion chalcogenide compounds [9].

Another interesting class of multianion compounds is the transition-metal oxyfluorides [10]. Oxygen and fluorine substitution presents the opportunity to create materials that possess the advantageous properties of both oxide and fluoride compounds. Transition-metal oxyfluorides have already shown improved performance over their oxide counterparts in electrochemical and solid-state lighting applications [11–14]. Moreover, other novel oxyfluoride compounds display a myriad of technologically useful properties, ranging from nonlinear optical behavior [15,16] to superconductivity [17,18].

From a chemical perspective, the oxide and fluoride ions appear to be quite similar. For instance, the closeness of their atomic number and ionic radii, i.e., 1.35 and 1.29 Å for  $O^{2-}$  and  $F^-$ , respectively [19], allows them to occupy the same sites in a crystal, making anion substitution easy. However, their differences in charge and electronegativity can lead to distinct physical properties in crystalline solids. The union of these contrasting traits in oxyfluoride anionic groups, i.e.,  $[MO_xF_{6-x}]^{n-}$ , where  $M$  is a (transition)-metal center, results in complex bonding interactions compared to compounds where only oxygen or fluorine are present. Specifically, the  $2p$  orbitals of the more electronegative fluoride anions are located deeper in the valence band compared to the same  $2p$  states of the oxide ions. When both anions belong to the same coordination sphere, the  $M-O$  bonds tend to display stronger

\*jrondinelli@northwestern.edu

covalent interactions with shorter bond lengths compared to the longer  $M$ -F bonds [20]. The result is oxyfluoride anionic groups with varying degrees of covalency within the same coordination sphere. The efficacy of different DFT  $V_{xc}$  approximations in describing oxyfluorides remains to be systematically assessed.

In this work, we evaluate the performance of exchange-correlation functionals at four rungs of Jacob's ladder, i.e., the local density approximation (LDA), generalized gradient approximation (GGA) as implemented by the Perdew-Burke-Ernzerhof functional for solids (PBEsol), metaGGA (MS2 and SCAN), and Heyd-Scuseria-Ernzerhof hybrid functional (HSE06) level which includes fractions of exact exchange. We focus on the accuracy of each  $V_{xc}$  potential in predicting the structural, electronic, and lattice dynamical properties in oxyfluorides. Specifically, we investigate how the approximations perform as the relative covalency increases by increasing oxygen content across 19 known fluoride, oxyfluoride, and oxide materials. Here we categorize each compound by the composition  $x$  of the local ligand chemistry about the octahedrally coordinated metals forming the anionic groups  $[MO_xF_{6-x}]^{n-}$  in the solid. Owing to the so-called chemical intuition derived from the  $\alpha$  parameter found in modern metaGGAs such as MS2 and SCAN, we expect them to be optimally suited to capture the subtleties of the oxyfluoride chemistry in the solid state. Our main finding is that PBEsol is the most suitable functional for calculating the structural properties, regardless of oxygen composition. In addition, we find that the inclusion of the kinetic energy in the metaGGAs MS2 and SCAN introduces functional dependencies, which deviate from trends previously reported for LDA, GGA, and hybrid functionals.

## II. METHODS AND MATERIALS SUITE

### A. Computational details

We performed density functional theory calculations as implemented in the Vienna *Ab initio* Simulation Package (VASP) [21,22] with the projector augmented wave (PAW) method [23] to treat the interactions between the core and valence electrons. The atomic reference configurations are  $2s^22p^4$  for the O and  $2s^22p^5$  for F in all compounds studied. The PAW atomic configurations of the cations, appearing in each compound, are tabulated in Ref. [24]. We also performed a series of convergence tests using different Monkhorst-Pack  $k$ -point meshes [25] and plane-wave cutoffs to find the appropriate values for each chemistry [24]. Full structural optimizations are performed until the Hellmann-Feynman forces are less than  $5 \text{ meV } \text{\AA}^{-1}$ . The phonon modes are analyzed using the PHONOPY package [26].

Here we note that Fuchs *et al.* showed that the distinct behavior of the core-valence exchange-correlation contributions in the LDA and GGA formalisms requires pseudopotentials to be tailored to calculations at each level of theory [27]. In particular, differences in core-valence overlap substantially affect the binding properties of solids [27]. With this understanding, we perform the LDA and PBEsol calculations with the respective VASP LDA and PBE-optimized PAWs. Because the hybrid- $V_{xc}$  HSE06 is a PBE-based functional, we also use

PBE-optimized PAWs in these calculations. At present, VASP does not support PAWs specifically optimized for metaGGA functionals; however, the newest PAWs distributed with the VASP.5.X package include information on the kinetic energy density of the core electrons that can be utilized in metaGGA calculations. Therefore, we also use PBE-optimized PAWs for all calculations using metaGGA exchange-correlation potentials.

### B. $V_{xc}$ performance trends in solids

DFT benchmarks of various solid-state materials have been successful in identifying the general *habits* of exchange-correlation functionals at different rungs of Jacob's ladder [28]. The local density approximation (LDA) and generalized gradient approximation (GGA) are at the first and second rung of the ladder, respectively. The XC energy density in the LDA is designed to mimic the density of the uniform electron gas [29]. LDA works well for simple metallic solids; however, it also has a tendency to overestimate cohesive energies of ionic solids and transition-metal complexes [30]. The failure of LDA to treat complex bonding interactions results in equilibrium volumes that are too small for most solids.

GGA improves on LDA by incorporating gradient corrections of the density [31–33]. One of the most widely used GGAs among materials researchers is based on the parametrization by Perdew, Burke, and Ernzerhof (PBE) [34,35]. Although it corrects the overbinding errors of the LDA, PBE tends to give bond lengths and cell volumes that are too large. For solids, the overestimation of cell volumes is significantly improved by other GGA functionals such as PBEsol, Wu-Cohen (WC), and SG4 [36–38].

The semilocal metaGGAs form the third rung of Jacob's density functional ladder and include the kinetic energy density of the Kohn-Sham orbitals as an additional ingredient. MetaGGAs strive to be more accurate than the GGA for a wider range of applications and chemical systems. Indeed, metaGGAs such as Tao-Perdew-Staroverov-Scuseria (TPSS) have proved to be more accurate than PBE in predicting the properties of bulk solids and surfaces [39,40]. However, TPSS often fails to capture the van der Waals' bonding in layered compounds such as graphite [41]. The inconsistencies of early metaGGAs were due in part to the inability of the dimensionless variables built from the kinetic energy to distinguish among different types of chemical bonding [3,42–44]. One way modern metaGGAs attempt to circumvent this problem is by tuning the kinetic energy density through a dimensionless parameter  $\alpha = [1/\text{ELF} - 1]^{1/2}$  (ELF is defined as the electron localization function; cf. Refs. [45,46]). The  $\alpha$  parameter characterizes the extent of orbital overlap throughout the crystal and thus is expected to enable modern metaGGAs to *intuitively* distinguish between a variety of bonding situations [42]. In addition,  $\alpha$  is essential for describing the asymptotic properties of the exchange energy density and exchange potential [47,48]. However, including the  $\alpha$  parameter is not essential to functional development and to the overall accuracy of modern metaGGAs because accurate metaGGAs can be constructed without the so-called  $\alpha$  parameter, for example, M06-L [49] and the recent

Tao-Mo (TM) metaGGA [50]. Although the modern metaGAs such as MS2 [43] and SCAN [40] show great promise, they have not been as extensively investigated as LDA, GGAs, or the hybrid functionals, which appear at the next rung [39,51].

Hybrid functionals mix semilocal XC (often from the GGA) with some contribution of exact exchange [52]. The goal of hybrid  $V_{xc}$  functionals is to produce more accurate thermochemical, magnetic, and electronic properties by mimicking the effects of static correlation [4,52–54]. The most popular hybrids, Becke three-parameter Lee-Yang-Parr (B3LYP) [52] and HSE06 [55], include approximately 20% to 25% exact exchange; however, studies have shown that this value is not unique and can be tuned to improve the accuracy of the desired property, such as the equilibrium geometry or electronic band gap [54,56–58]. Notably, hybrid functionals overcome a major shortcoming of the nonempirical semilocal functionals in that they *cannot* provide accurate band gaps beyond the exact Kohn-Sham gap. For semilocal functionals, this often results in a significant underestimation of the electronic band gap in solids. In fact, correlated transition-metal compounds are often gapless at these levels of theory. DFT calculations using hybrid functionals often predict band-gap values that are much closer to experiment, marking a significant improvement over semilocal functionals. However, the inclusion of exact exchange comes at significantly greater computational cost compared to the approximations at lower rungs, particularly in DFT codes based on plane-wave basis sets.

### C. Compounds and crystal data

Figure 1 shows the crystal structures for the 19 compounds investigated, which belong to either the fluoride, oxyfluoride, or oxide families. The materials can be further delineated by considering the ratio of oxygen  $x$  to fluorine  $6 - x$  within the octahedral anionic groups comprising the structure, i.e.,  $[MO_xF_{6-x}]^{n-}$ , where  $x$  is an integer ranging from 0 to 6. We note that all phases examined have been experimentally synthesized and both the cation-site and anion sublattices are fully ordered with no cation-site or anion-site intermixing. All crystallographic data for the DFT optimized structures are provided in the Supplemental Material [24].

For the fluorides with  $MF_6$  ( $x = 0$ ) octahedra, we study six compounds belonging to four crystal families. KF is a simple binary fluoride with the  $AB$  rock-salt structure [59].  $VF_2$  [60] and  $MnF_2$  [61] exhibit the  $AB_2$  rutile structure.  $KMnF_3$  [62] exhibits the  $ABX_3$  perovskite structure, whereas  $Na_3ScF_6$  [63] and  $Na_3MnF_6$  [64] are ordered double perovskites with the cryolite structure—Na occupies both the  $A$  and  $B$  positions in the  $A_2B_2X_6$  structure [65].

By inspection of Fig. 1, we find that ordered [66–75] oxyfluorides ( $x = 1, \dots, 5$ ) crystallize in a wide variety of structure types with corner, edge, and face connectivity among polyhedral units. As an illustration of our schema to differentiate the oxyfluorides using the local  $[MO_xF_{6-x}]^{n-}$  anionic groups rather than the usual chemical formula, consider  $Ba_2WO_3F_4$  and  $NaNbO_2F_2$ . Although these compounds have different chemical formulas, they both exhibit  $MO_4F_2$

octahedral units, i.e.,  $[WO_4F_2]^{4-}$  and  $[NbO_4F_2]^{5-}$ , and thus are grouped together in Fig. 1.

Last, we study two ternary oxides with  $MO_6$  ( $x = 6$ ) octahedra: the perovskites  $SrTiO_3$  [76] and  $BaTiO_3$  [77] with distorted tetragonal configurations, i.e., non-polar  $I4/mcm$  (with out-of-phase  $TiO_6$  octahedral rotations) and polar  $P4mm$  (with an electric polarization), respectively.

All 19 compounds are electronic insulators, with 15 of the 19 compounds investigated nonmagnetic  $d^0$  insulators. The antiferromagnetic compounds  $VF_2$  ( $d^3$ ),  $MnF_2$  ( $d^5$ ), and  $KMnF_3$  ( $d^5$ ) are Slater insulators [78,79]. Here we simulate  $VF_2$ ,  $MnF_2$ , and  $KMnF_3$  with C-type magnetic order [80].  $Na_3MnF_6$  ( $d^4$ ) is known experimentally to be insulating; however, the magnetic properties have not been thoroughly explored [64]. In our previous work, we established that  $Na_3MnF_6$  exhibits a weak energetic preference for ferromagnetic spin order over an antiferromagnetic spin configuration [81]. Because these four magnetic compounds are Slater insulators, we are able to assess the performance of each XC functional without requiring a Hubbard- $U$  correction to ensure insulating behavior [82,83].

## III. RESULTS

### A. Structure analysis

#### 1. Cell volume

Figure 2 shows the percentage error (% error) in the cell volume  $\Omega$  obtained from DFT with the different XC functionals relative to the experimentally (expt) measured structures at room temperature, which is obtained as % error =  $(\Omega_{XC} - \Omega_{expt})/\Omega_{expt} \times 100$ . First, we observe the well-known overbinding of LDA for all compounds. The underestimation in the cell volume is larger than 3% across all chemistries, with the exception of  $SrTiO_3$  where the discrepancy is 2.3%.

In contrast, cell optimizations with XC functionals at rungs higher than LDA show increased accuracy (errors  $\lesssim 3\%$ ). The GGA PBEsol performs well, consistently predicting cell volumes to within 2% error, with a slight tendency towards overbinding (Fig. 2). Our results also show that the hybrid functional HSE06, appearing at the highest rung of Jacob's ladder, more frequently overestimates the cell parameters than the other functionals. This result is consistent with what has been previously reported for perovskite oxides studied using either HSE06 or the unscreened hybrid PBE0 [30,57]. We find that HSE06 gives the best overall performance for the ionic all-fluoride  $MF_6$  ( $\sim 1\%$ ) and more covalent all-oxide  $MO_6$  ( $\sim 0.5\%$ ) compounds. Surprisingly, our results suggest that the degree of unit-cell overestimation is often greater for the oxyfluorides with  $MO_xF_{6-x}$ ,  $x = 1, \dots, 5$ , where errors  $> 1.5\%$  are found.

At the metaGGA level, we investigate the MS2 and SCAN functionals (Fig. 2). First, our structural optimizations with MS2 reveal comparable and sometimes better accuracy than PBEsol ( $\sim 2\%$ ), particularly for the all-fluoride  $MF_6$  compounds. Although MS2 shows a strong tendency to underestimate the volumes of the fluorides, a consistent trend is less clear across the oxyfluorides and oxide compounds. Next, our results indicate that SCAN produces smaller cell

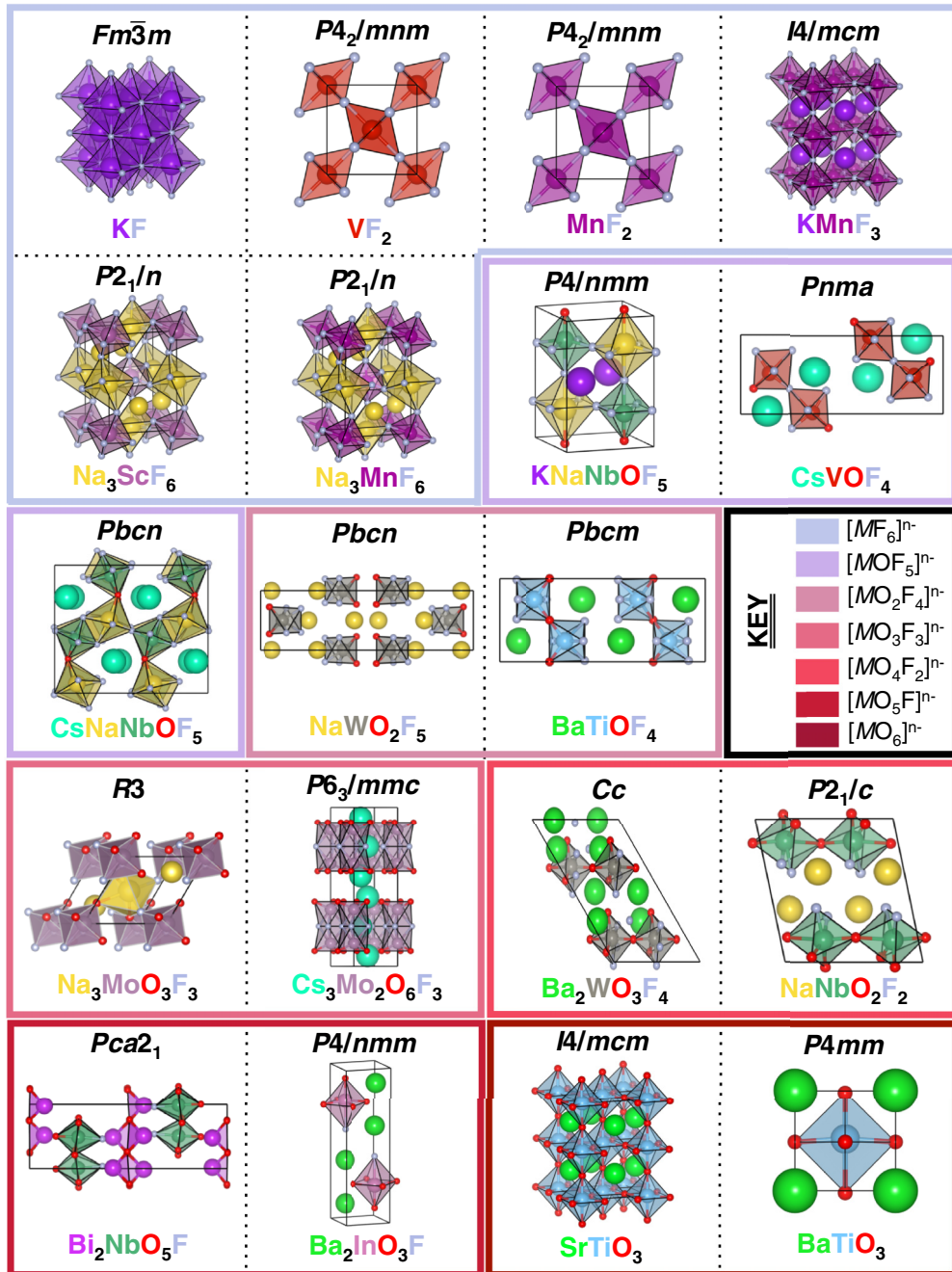


FIG. 1. Crystal structures of the 19 compounds appearing in this study. The structures are grouped based on the oxygen/fluorine ratio in the  $[MO_xF_{6-x}]^{n-}$  anionic group. Each anionic group can be differentiated by the colors bordering the structures, as indicated in the key (black outlined panel), and this color scheme is used in all subsequent figures to differentiate anionic groups.

volumes across all chemistries and is often less accurate than MS2, particularly in predicting  $\Omega$  of the more ionic compounds ( $MO_xF_{6-x}$ ,  $x = 0, 1, 2$ ) with an error  $\sim 3\%$ . These results are inconsistent with a recent study reported by Sun *et al.* [40] and we conjecture two factors may be responsible for the poorer performance herein:

(i) Finite-temperature effects, i.e., the experimental structures for which we assess the XC functional accuracy, are measured at room temperature and thus must be zero-point corrected. This is germane to all volumes calculated with any XC functional.

(ii) Maladapted PBE PAWs resulting in inaccurate core-valence exchange and correlation for the metaGGA functionals.

First, we investigate the contribution of thermal expansion for KF,  $Na_3ScF_6$ , and  $BaTiO_3$  to address inaccuracies derived from missing finite-temperature contributions in Fig. 2. From the measured coefficient of thermal expansion (CTE) for  $BaTiO_3$ , we approximate that the material will contract by 0.19% at 0 K [84]. For KF and  $Na_3ScF_6$ , we compute the CTE with a self-consistent quasiharmonic approach at the PBEsol level [85]. We observe that the effect of zero-point

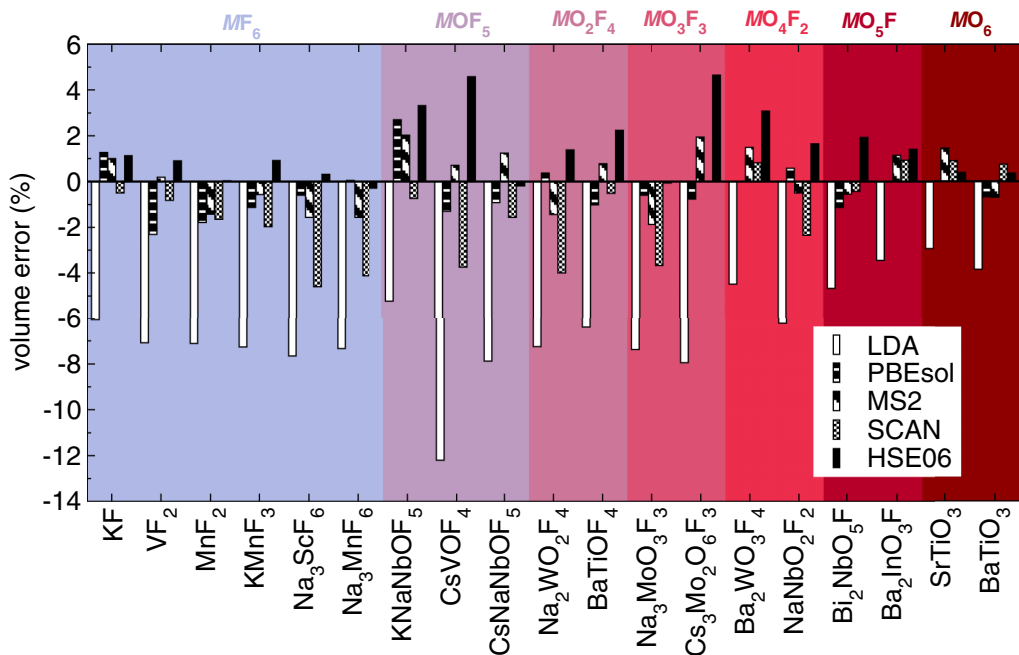


FIG. 2. Percent error in DFT computed cell volumes relative to experiment obtained using different exchange-correlation potentials as indicated by the different shaded bars. The  $MO_xF_{6-x}$  octahedra present in each compound are shown on the upper abscissa, differentiated by shaded regions.

volume correction is much larger for the fluorides with volume changes of approximately 1.3% and 1.7% for KF and  $Na_3ScF_6$ , respectively. This result suggests that the effects of thermal expansion may be more significant for compounds comprised of  $MF_6$  rather than  $MO_6$  octahedra. Although the zero-point correction improves the calculated metaGGA volumes compared to experiment, it alone does not fully account for the observed discrepancies, particularly in the case of  $Na_3ScF_6$ .

Next, we investigate the equilibrium volume dependence on the electronic configuration of the PAW pseudopotential (all based on PBE exchange and correlation) for three XC functionals. Here we vary the cations' valence electronic configuration in the KF,  $Na_3ScF_6$ , and  $BaTiO_3$  compounds as a means to perturb the core-valence exchange-correlation interaction owing to the unavailability of PAWs constructed specifically for metaGGA functionals.

Table I presents the volume errors for PBEsol, MS2, and SCAN as a function of cation PAW choice. We observe that the computed  $BaTiO_3$  volumes show little sensitivity to the form of the Ti PAW. All three XC functionals result in volume errors  $<1\%$  compared to experiment. In contrast, a change in the PAW electronic configuration has a pronounced effect on the equilibrium volume in both the  $MF_6$  containing compounds KF and  $Na_3ScF_6$ . Moreover, the computed volumes obtained from SCAN and MS2 show a much larger variance than PBEsol when more or fewer electrons are included as valence. These results suggest that the optimized PBE PAWs may not be “totally” transferable to modern metaGGAs such as MS2 and SCAN. We believe that a more in-depth study following that of Fuchs *et al.* [27], which compares the role of pseudopotential choice on the accuracy of metaGGAs, may be necessary before ultimately drawing schematic conclusions on its performance across many material classes.

To understand the performance of the XC functionals as the relative covalent bonding active in the compounds evolves from the ionic fluorides to the more covalent oxides, we plot the root-mean-squared (RMS) error in the cell volume for each material in our test suite with respect to anionic composition  $MO_xF_{6-x}$ , ( $x = 0, \dots, 6$ ) ratio (Fig. 3). Our statistical analysis confirms the previously stated results, i.e., the LDA is the least accurate and HSE06 performs the best for fluorides and oxides. However, it also reveals other less obvious trends described next.

TABLE I. The cell-volume error (%) for KF,  $Na_3ScF_6$ , and  $BaTiO_3$  optimized with DFT using different PBE cation PAW valence configurations from three different exchange-correlation functionals: PBEsol, MS2, and SCAN. The computed volumes are compared to the experimentally measured volumes at room temperature.

Solid	PAW	PBEsol	MS2	SCAN
KF	K, $3p^64s^1$	1.26	1.00	-0.50
	K, $3s^23p^64s^1$	1.13	-0.19	-3.10
$Na_3ScF_6$	Na, $3s^1$			
	Sc, $3d^24s^1$	-4.98	-6.38	-8.73
	Na, $2p^63s^1$			
	Sc, $3d^24s^1$	-1.69	-3.38	-5.46
	Na, $3s^1$			
	Sc, $3s^23p^63d^24s^1$	-4.25	-5.12	-7.85
$BaTiO_3$	Na, $2p^63s^1$			
	Sc, $3s^23p^63d^24s^1$	-0.60	-1.57	-4.57
	Ba, $5s^25p^66s^2$			
	Ti, $3p^63d^34s^1$	-0.68	-0.70	-0.75
	Ba, $5s^25p^66s^2$			
Ti, $3s^23p^63d^34s^1$	-0.87	-0.60	-0.62	

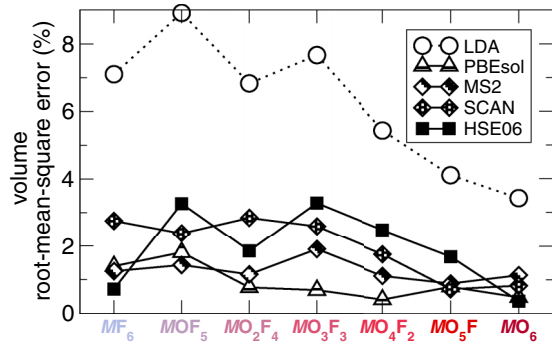


FIG. 3. RMS error in volume with different  $V_{xc}$  potentials as a function of increasing oxygen content,  $x = 0$  (left) to  $x = 6$  (right), within the  $MO_xF_{6-x}$  anionic units.

Notably, we observe that the unit-cell volumes predicted by all functionals become more accurate as the relative covalency of the material increases, i.e., with increasing oxygen content  $x$  in the anionic group. LDA shows the most noticeable improvement across the series, with the RMS error changing from 7% and 9% for  $MO_xF_{6-x}$  with  $x = 0$  and 1, respectively, to 3.1% for the oxides ( $x = 6$ ). Interestingly, we observe that across all O-to-F ratios, the PBEsol functional provides the most consistent performance and is overall the most accurate for the intermediate anion ratios exhibited by the  $MO_xF_{6-x}$ ,  $x = 2, 3$ , and 4 oxyfluorides. Last, we find that between the metaGGAs, MS2 exhibits better overall performance than SCAN (Fig. 3). We observe that the RMS error of SCAN is significantly better for the oxides compared to the fluorides, which suggests that it may be better suited to describe the more pronounced covalent bonding interactions oxides and chalcogenides.

## 2. Internal coordinates

Next, we assess the effectiveness of each XC functional at accurately predicting the internal ionic positions compared to those reported in the experimental structures. In Fig. 4, we report the structural arithmetic mean introduced in Ref. [86] to assess the likeness of two structures, and defined as  $d_{av} = (\sum_i m_i u_i)/n$ , where  $i$  is the index of the occupied Wyckoff site,  $m_i$  is the multiplicity of the Wyckoff orbit in the unit cell,  $u_i$  represents the atomic displacement amplitude required to map one structure onto another, and  $n$  is the total number of atoms in the unit cell. Note that an arithmetic mean of  $d_{av} = 0$  Å corresponds to perfect agreement between two structures. In this definition, the cell strain contribution is omitted.

**Fluorides.** The structure of KF has  $Fm\bar{3}m$  symmetry and no free internal parameters for the occupied Wyckoff positions. As a result, the arithmetic mean for KF is zero.  $VF_2$  and  $MnF_2$  exhibit the rutile structure ( $P4_2/mnm$ ) and thus have two positional degrees of freedom for the fluoride ion located on the  $4f$  Wyckoff site. We find that the predicted equilibrium atomic positions obtained from all  $V_{xc}$  functionals generally match closely with the experimental rutile structures. For example, in  $VF_2$ , we find that the error is quite similar at all levels of theory (Fig. 4); however, for  $MnF_2$ , we observe that the predicted internal coordinates are systematically improved as we climb Jacob’s ladder.

The perovskite structured  $KMnF_3$ ,  $Na_3ScF_6$ , and  $Na_3MnF_6$  compounds exhibit corner-connected  $MF_6$  octahedral units that rotate about several crystal directions. The main distortion in  $KMnF_3$  is an out-of-phase rotation of the fluoride octahedra about the  $[001]$  direction (of  $2.6^\circ$ ), which corresponds to two free internal positions for the fluoride anion ( $8h$  Wyckoff site). Figure 4 shows that the LDA gives the poorest performance (angle of  $8.2^\circ$ ) in predicting the internal positions, followed by SCAN ( $8.0^\circ$ ), HSE06 ( $7.4^\circ$ ), PBEsol ( $6.5^\circ$ ), and MS2 ( $5.1^\circ$ ).

The primary distortions in the double perovskites  $Na_3ScF_6$  and  $Na_3MnF_6$  are out-of-phase fluorine octahedral rotations about the  $[110]$  direction ( $\phi$ ) and an in-phase rotation about  $[001]$  ( $\theta$ ). From Fig. 4, we observe that in general all functionals perform slightly better for the double perovskites than  $KMnF_3$ . The amplitudes of the octahedral rotations in the double perovskites ( $Na_3ScF_6$ :  $\phi = 21.1^\circ$ ,  $\theta = 13.3^\circ$  and  $Na_3MnF_6$ :  $\phi = 19.4^\circ$ ,  $\theta = 12.5^\circ$ ) are much larger compared to the amplitude of the rotation in  $KMnF_3$ . We find that the amplitudes of the in-phase and out-of-phase rotation angles are within  $1\text{--}2^\circ$  (cf. Ref. [24]) of the experimental values for all functionals studied.

The increased accuracy of the predicted rotations is likely responsible for the improved performance of the XC functionals for the double perovskite over  $KMnF_3$ . For these ternary fluorides, the LDA functional remains the least accurate at predicting the internal coordinates. For  $Na_3ScF_6$ , we note that the arithmetic mean obtained for the nonhybrids PBEsol and MS2 performs slightly better than HSE06; however, the metaGGA SCAN is the worst performer among the functionals for  $Na_3ScF_6$ . On the other hand, PBEsol and HSE06 are found to be the most accurate for  $Na_3MnF_6$ . Mode-crystallographic analysis between the ground-state monoclinic double-perovskite structures and the ideal high-symmetry parent  $Fm\bar{3}m$  lattice reveals that  $Na_3ScF_6$  and  $Na_3MnF_6$  have complex atomic distortions (see Ref. [81] for full description). By comparing the symmetry-adapted mode amplitudes for  $Na_3ScF_6$  and  $Na_3MnF_6$  (see Ref. [24]), we observe that discrepancy in the internal coordinates is predominately due to the inaccuracy in predicting secondary distortions as opposed to octahedral rotations.

**Oxyfluorides.** The oxyfluoride compounds studied here belong to a diverse set of structure types, with different polyhedral connectivity. Our results do not reveal a clear trend in the accuracy of the calculated internal coordinates from difference  $V_{xc}$  potentials as a function of increasing oxygen content in the anionic unit. However, from Fig. 4, we can conclude that the LDA is most often the least accurate functional in predicting the internal coordinates regardless of oxygen content and thus should be avoided.

One anomalous result we find is the significant arithmetic means, corresponding to possible large errors in the optimized atomic positions, for the compounds  $CsVOF_4$  (with  $[VOF_5]^{2-}$ ) and  $Bi_2NbO_5F$  (with  $[NbO_5F]^{6-}$ ). To understand the origin of this behavior, we compare the global instability index (GII) of the experimental structures and the DFT optimized geometries for each material. The GII judges the “plausibility” of a crystal structure based on the deviation of the bond valence sums of the constituent ions from their formal valence averaged over all atoms in the unit cell [87,88]. Using this metric, crystal structures that are characterized by  $GII > 0.2$  valence units

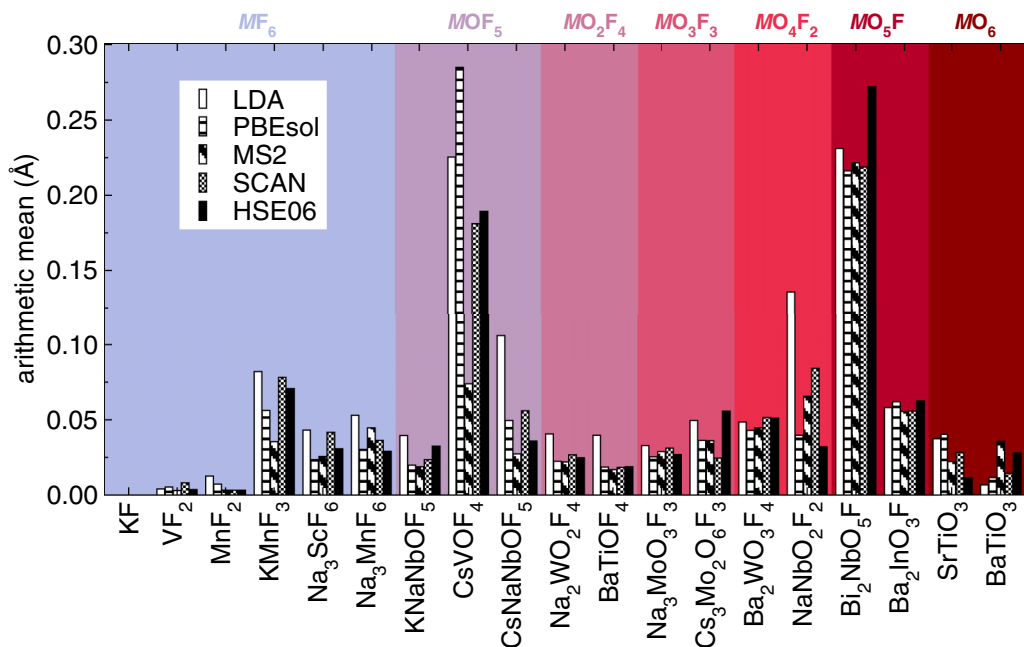


FIG. 4. Error in internal coordinates of DFT computed structures relative to experiment obtained using different XC functionals indicated by shaded bars. The anionic group present in each compound is shown on the upper abscissa differentiated by shaded regions. An arithmetic mean of  $d_{av} = 0 \text{ \AA}$  indicates perfect agreement, which occurs for KF because by symmetry there are no free internal positions.

(v.u.) either show evidence of strained bonds or an incorrectly reported structure.

For  $\text{CsVOF}_4$ , we calculate a GII value of 0.203 v.u. for the experimentally reported structure, which is close to the boundary of a material exhibiting large bond strains. Further analysis of the experimental structure reveals that the large GII is due to compressed V-O and V-F bonds in the  $[\text{VOF}_5]^{n-}$  units compared to the bond valence parameters. Figure 1 in the Supplemental Material [24] shows that the DFT optimized structures, with the exception of that obtained from the LDA, reduce the GII to  $<0.14$  v.u. (see Ref. [24]). Therefore, we contend that the large discrepancies for  $\text{CsVOF}_4$  observed in Fig. 4 result from the comparison with an experimental structure with strained bonds. We observe that the cell optimizations with PBEsol, HSE06, and the metaGGAs increase the  $[\text{VOF}_5]^{n-}$  polyhedral volumes and reduce the strain on the bonds observed in the experimental structure. Our results suggest that the internal coordinates of the  $\text{CsVOF}_4$  experimental structure may require reassessment.

We calculate  $\text{GII} = 0.260$  for the experimental  $\text{Bi}_2\text{NbO}_5\text{F}$  structure. All functionals besides the LDA are found to reduce the strain in the stretched Bi-O bonds of the experimental structure [24]. However, unlike  $\text{CsVOF}_4$ ,  $0.2 < \text{GII} < 0.26$  v.u. for all structures obtained with the different XC functionals, except from the LDA. This result also suggests that the internal coordinates of  $\text{Bi}_2\text{NbO}_5\text{F}$  may need to be revisited.

*Oxides.* The tetragonal perovskite oxides  $\text{SrTiO}_3$  and  $\text{BaTiO}_3$  are found in space groups  $I4/mcm$  and  $P4mm$ , respectively. For  $\text{SrTiO}_3$ , the experimental out-of-phase  $\text{TiO}_6$  rotation angle is  $\approx 2.1^\circ$  about the  $[001]$  direction. LDA and PBEsol both predict the out-of-phase angle to be  $\sim 5^\circ$ , whereas the metaGGAs perform slightly better, i.e., MS2 gives  $3.7^\circ$  and SCAN gives  $4.1^\circ$ . HSE06 performs most accurately

for  $\text{SrTiO}_3$ , providing an equilibrium rotation angle of  $2.9^\circ$ . This result is consistent with the findings of Aramburu and co-workers, who proposed that the subtle energy variations associated with octahedral rotations are a more stringent test of the predictive capabilities of exchange-correlation functionals compared to strain tensors in structurally complex materials [57]. They argue that the accuracy of the hybrid functionals derives from the pseudo-Jahn-Teller vibronic contribution to octahedral tilting in semicovalent solids [89]. Specifically, the larger band gaps predicted by hybrid functionals such as HSE06 reduce the covalent interactions between occupied and unoccupied orbitals, which manifest through electron-lattice interactions, thus resulting in smaller predicted rotation angles [57].

Figure 4 shows that  $d_{av}$  of the polar oxide  $\text{BaTiO}_3$  increases as we climb Jacob's ladder. To understand this trend, we examine the ferroelectric displacements in  $\text{BaTiO}_3$  and focus on the Ti off centering. Prior studies have established that the amplitude of the ferroelectric distortion in  $\text{BaTiO}_3$  is strongly linked to the equilibrium cell volume as determined by the selected exchange-correlation functional, e.g., LDA, GGA, or hybrid [30,91,92]. Variable cell and atomic relaxations with  $V_{xc}$  functionals that favor larger unit-cell volumes predict larger ferroelectric displacements, thus suggesting no direct functional dependence of the ferroelectric distortion in  $\text{BaTiO}_3$ , but rather that the dependency originates from indirect errors in the cell volume.

In Fig. 5, we plot the displacement of the Ti ion from the  $(\frac{1}{2}, \frac{1}{2}, \frac{1}{2})$  position with Ba at the origin and the  $c/a$  lattice parameter axial ratio as a function of optimized equilibrium volume for each XC functional. We observe that the  $V_{xc}$ -volume dependence reported in previous studies is maintained by the LDA, PBEsol, SCAN, and HSE06 functionals and that the  $c/a$  ratio obeys a similar trend to the Ti ion displacement

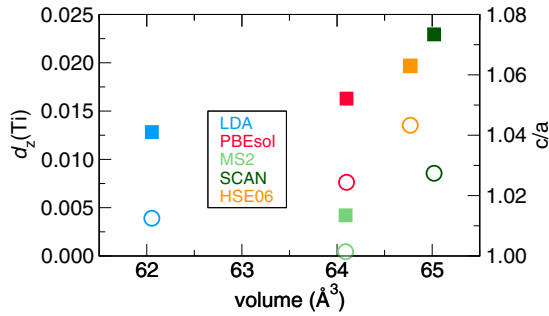


FIG. 5. The Ti ion displacement  $d_z(\text{Ti})$  along the [001] direction (filled symbols) and corresponding axial ratios (empty symbols) in tetragonal  $P4/mmm$   $\text{BaTiO}_3$  as a function of optimized unit-cell volumes obtained with different exchange-correlation potentials. Experimentally,  $d_z(\text{Ti}) \sim 0.015$  (Ref. [90]).

as a function of optimized cell volume for LDA, PBEsol, and HSE06, i.e.,  $c/a$  increase with larger cell volume. However, the metaGGA functionals, MS2 and SCAN, deviate from these trends. First, MS2 predicts an optimized cell volume for  $\text{BaTiO}_3$  that is nearly identical to PBEsol, yet exhibits a Ti displacement that is nearly three times smaller. We can understand this by examining the  $c/a$  ratio obtained from MS2. The lattice tetragonality for  $\text{BaTiO}_3$  is nearly quenched with MS2 (Fig. 5). In the case of SCAN, we observe that although the functional predicts the largest optimized cell volume, the  $c/a$  ratio obtained is only slightly larger than the PBEsol value. These results strongly suggest that the inclusion of the kinetic energy density in metaGGAs introduces a direct functional dependence for the ferroelectric distortion in  $\text{BaTiO}_3$ . Based on these findings, we recommend that when these modern

metaGGAs are used to study and predict new ferroelectric compounds, a detailed structural analysis is essential.

**B. Electronic properties**

We now compute the electronic density of states (DOS) for each compound optimized with each XC functional. The calculated electronic gaps are reported in Fig. 6. Owing to a shortage of experimental data on the band gaps of most of the compounds in this study, we are unable to provide a direct assessment of the accuracy of each functional against experiment. Qualitatively, we anticipate the relative size of the band gap to decrease as fluorine is replaced with the less electronegative oxide anion. Indeed, Fig. 6 demonstrates that this trend is observed for the  $d^0$  compounds regardless of the choice of  $V_{xc}$ .

First we find that the DFT band gap increases as one climbs Jacob’s ladder of exchange-correlation functionals (Fig. 6). As expected, the LDA and PBEsol give the smallest band gaps and HSE06 gives the largest band gap for all compounds, regardless of oxygen content  $x$  in the  $\text{MO}_x\text{F}_{6-x}$  octahedra. In addition, both metaGGAs, i.e., MS2 and SCAN, show larger band gaps than the LDA and GGA as observed in other binary semiconductors including GaAs and CaO [96], with SCAN always producing larger band gaps than MS2.

**C. Lattice dynamical properties**

Now we investigate the  $V_{xc}$ -dependent lattice vibrational frequencies. We compute the phonons at the optimized theoretical volumes with each level of theory and report the transverse optical frequencies. Given the high computational cost of accurate phonon calculations and the scarcity of experimental vibrational data for most compounds in this study, we focus

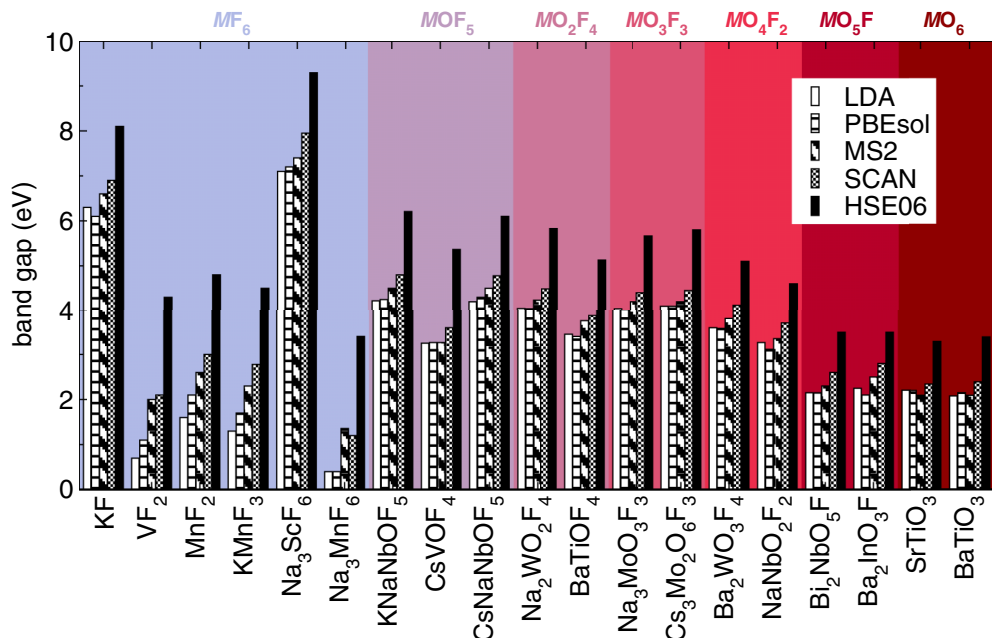


FIG. 6. Electronic band-gap evolution with variable oxygen content  $x$  in the  $\text{MO}_x\text{F}_{6-x}$  octahedra from different exchange-correlation functionals (shaded bars). The anionic group present in each compound is shown on the upper abscissa differentiated by shaded regions. The experimental measured gap for KF is 10.8 eV [93].  $\text{SrTiO}_3$  has a measured direct  $\Gamma-\Gamma$  band gap of 3.75 eV and an indirect  $R-\Gamma$  gap of 3.25 eV [94]. The experimental band gap of  $\text{BaTiO}_3$  is 3.4 eV [95].

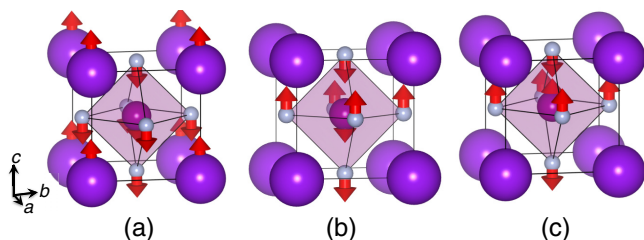


FIG. 7. Eigendisplacements (red arrows) for the IR-active transverse-optical (TO) modes (a) TO1, (b) TO2, and (c) TO3 in cubic  $Pm\bar{3}m$   $KMnF_3$ .

on four representative materials that sample the range of O/F concentrations observed in the material suite:  $KMnF_3$  ( $x = 0$ ),  $KNaNbOF_5$  ( $x = 1$ ),  $Na_2W_2F_4$  ( $x = 2$ ), and  $Na_3MoO_3F_3$  ( $x = 3$ ). With regards to the oxide only containing compounds ( $x = 6$ ),  $BaTiO_3$  and  $SrTiO_3$ , we note that a prior study by Kresse *et al.* has already established the phonon functional dependence and therefore we do not repeat it here [30].

The fluoroperovskite  $KMnF_3$  is cubic ( $Pm\bar{3}m$ ) at room temperature [97]. Here we investigate the  $\Gamma$ -point phonon frequencies of the cubic phase, which like other perovskites consists of four triply degenerate transverse-optical (TO) modes. Three of the TO modes are infrared (IR) active (Fig. 7) [98]. In Fig. 8, we plot the computed IR mode frequencies vs volume at four rungs of DFT alongside available experimental data [99]. We find that all XC functionals perform well, providing calculated TO-mode frequencies close to experiment at the respective

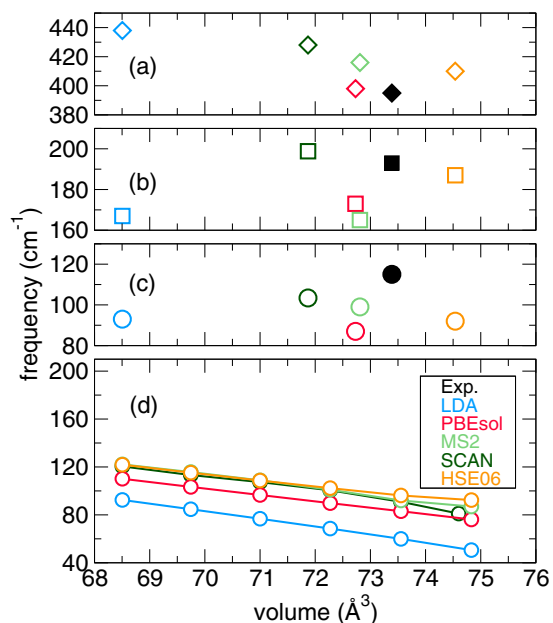


FIG. 8. Infrared frequencies computed different cell volumes with the LDA, PBEsol, MS2, SCAN, and HSE06 functionals for cubic  $KMnF_3$ . (a)–(c) The computed frequencies of the (a) TO3 mode, (b) TO2 mode, and (c) TO1 mode are plotted at respective equilibrium volume for each functional. (d) The evolution of the TO1 mode frequency as a function of cell volume for each functional. The empty diamond, square, and circular symbols represent the TO3, TO2, and TO1 modes, respectively.

equilibrium volume [Figs. 7(a)–7(c)]. Specifically, the TO1 mode is underestimated by every functional [Fig. 8(a)], while the TO2 mode is underestimated by every functional besides SCAN [Fig. 8(b)]. The frequency of the highest experimental IR mode frequency nearly coincides with that obtained from PBEsol [Fig. 8(c)].

In Fig. 8(d), we plot the evolution of the lowest-frequency IR-active mode as a function of the cubic cell volume. Our results demonstrate that the TO1 mode decreases almost linearly with increasing cell volume for all functionals investigated. We find that given the same cell volume, LDA always predicts a softer TO1-mode frequency, followed by PBEsol. The largest frequencies are predicted by the metaGGAs and HSE06. In fact, Fig. 8(d) shows that for the same cell volume, the TO1 modes obtained from the metaGGA and hybrid functionals are nearly identical. The trend of higher phonon frequencies obtained from hybrid- $V_{xc}$  functional calculations has been reported previously and is attributed to stiffer bonds owing to the inclusion of exact exchange [30]. Interestingly, despite having no exact exchange added, and predicting smaller optimized cell volumes, the metaGGAs behave nearly identically to HSE06 with respect to the mode frequencies.

We were unable to find experimental vibrational data for the ordered oxyfluoride compounds to use for a direct comparison with our calculations. However, we note that vibrational spectroscopy measurements are routinely used to help characterize local anion order in  $MO_xF_{6-x}$  complexes, especially in cases where the compounds appear disordered to x-ray diffraction [100,101]. In this regard, the  $M$ -O stretching mode is particularly important in identifying the nature of anion order in the octahedral environment, for example, when deciphering *cis* vs *trans* configurations for  $MO_2F_4$  units or *fac* vs *mer* configurations for  $MO_3F_3$  units. Our literature survey of  $[NbOF_5]^{2-}$ ,  $[WO_2F_4]^{2-}$ , and  $[MoO_3F_3]^{3-}$  anions revealed that the IR-active frequency of the  $M$ -O stretching mode appears in the 800–1000  $cm^{-1}$  range and was relatively insensitive to the choice of counter cations. For that reason, we investigate the functional dependence of the  $M$ -O mode frequency for the compounds  $KNaNbOF_5$ ,  $Na_2WO_2F_4$ , and  $Na_3MoO_3F_3$ . The DFT frequencies are compared to the statistical mean  $\sigma$  of the experimentally measured  $M$ -O frequencies for similar chemistries consisting of  $[NbOF_5]^{2-}$ , *cis*- $[WO_2F_4]^{2-}$ , and *fac*- $[MoO_3F_3]^{3-}$  octahedra.

Figure 9 shows that for these three oxyfluorides, the LDA, PBEsol, and MS2 functionals predict the  $M$ -O stretching mode with comparable accuracy compared to the experimental (literature) mean. Specifically, we observe that the mode frequencies computed by semilocal functionals are very similar, with LDA consistently predicting the largest frequency for all three compounds. The calculated PBEsol frequencies are slightly smaller than those obtained from MS2 for the compounds  $KNaNbOF_5$  ( $x = 1$ ) and  $Na_2WO_2F_4$  ( $x = 2$ ), whereas the values are nearly identical for  $Na_3MoO_3F_3$  ( $x = 3$ ). SCAN, on the other hand, predicts stiffer mode frequencies compared to the other semilocal functionals. In addition, we observe that  $M$ -O mode frequencies calculated with the hybrid HSE06 are often harder than the semilocal functional predictions. We also note that the overestimation of the  $M$ -O mode frequency by HSE06 decreases as the percent overestimation of the cell volume is reduced (cf. Fig. 2).

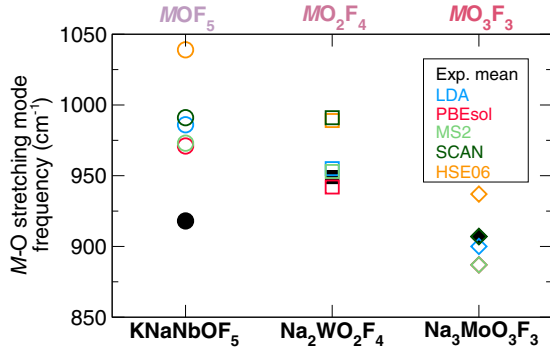


FIG. 9. Infrared frequencies for the  $M$ -O stretching mode in  $\text{KNaNbOF}_5$ ,  $\text{Na}_2\text{WO}_2\text{F}_4$ , and  $\text{Na}_3\text{MoO}_3\text{F}_3$  compared to the experimental mean of related compounds. Experimental phonon frequencies taken from Refs. [15,100–105]. Note that the PBEsol result overlaps with MS2, and SCAN matches the experimental mean for  $\text{Na}_3\text{MoO}_3\text{F}_3$ .

The latter suggests that the increased frequency observed in our HSE06 calculations is strongly tied to the degree of overestimation of the cell volume.

In Table II, we summarize the deviation of the six computed phonon frequencies from experiment. We observe that PBEsol has the lowest mean absolute error of all functionals, while HSE06 has the highest. Between the metaGGA functionals, MS2 has a lower mean absolute error than SCAN. As we have already seen for  $\text{KMnF}_3$ , if given identical cell volumes, then the metaGGAs predict very similar mode frequencies to HSE06; therefore, this analysis further suggests that the major source of these discrepancies is due to the error in the optimized cell volume.

Our results are consistent with previous reports on the sensitivity of the phonon-mode frequencies with XC functionals in crystalline solids [3,30,91]. For the  $\text{MO}_x\text{F}_{6-x}$  ( $x = 0, 1, 2, 3$ ) fluorides and oxyfluorides studied here, we observe (i) that although there is some dependence of the phonon frequency on the choice of exchange-correlation functional, the accuracy of the computed phonon modes is most significantly affected by cell volume and (ii) the lower rung functionals can be as accurate as the metaGGA and hybrid functionals.

TABLE II. The mean absolute error (mean AE) and maximum absolute error (max AE) from experiment of vibrational frequencies for the six modes (three IR modes of  $\text{KMnF}_3$  and  $M$ -O stretching mode of  $\text{KNaNbOF}_5$ ,  $\text{Na}_2\text{WO}_2\text{F}_4$ ,  $\text{Na}_3\text{MoO}_3\text{F}_3$ ) measured in this study. All values are in  $\text{cm}^{-1}$ . Error = theory – experiment. Mean AE =  $1/n \sum_{i=1}^n |\text{Error}|$ .

Method	Mean AE	Max AE
LDA	28.7	68
PBEsol	21.7	53
MS2	24.1	55
SCAN	27.6	73
HSE06	39.4	121

## IV. DISCUSSION

Our benchmark study systematically investigates the performance of different  $V_{xc}$  approximations within DFT at four different levels against oxygen content in a variety of oxyfluoride compounds. With the evolution of the oxygen-to-fluorine (O/F) ratio in these compounds, the implicit assumption is that the balance of covalency (or ionicity) of the solids would also evolve proportionally. Although the terms *ionic “bond”* and *covalent bond* can be defined, decades of debate has proved that there exists no unambiguous scale with which ionicity can be quantified, particularly as a bulk property [106–108]. Nevertheless, various ionicity scales have proved to provide useful approximations in a variety of applications [107,109–112].

Perhaps one of the most useful and transferable ionicity formalisms was introduced by Pauling [113]. His approach of using electronegativity differences as a measure of bond polarizabilities [19] between ions has proved accurate in describing the bonding in simple metal fluorides and oxide crystals [106]. Here we qualitatively assess the effect of increasing oxygen content in this materials suite by defining *% ionicity of a solid* as the weighted average ionicity obtained from all atomic pair electronegativity differences in the crystal as follows:  $\% \text{ ionicity} = (\sum w_{AB} f_{AB})/W$ , where  $f_{AB}$  is the ionicity of the bond between ions  $A$  and  $B$  according to Pauling’s electronegativity scale [113]. The weight of the interaction  $w_{AB}$  is computed by adding the site multiplicity of ions  $A$  and  $B$ , and  $W = \sum_i w_i$  is the sum of all the interaction weights. Using this approximation, we observe that decreasing ionicity does not directly correlate with a change in oxygen/fluorine ratio [Fig. 10(a)]. However, the general behavior of this metric shows that the fluorides and oxides cluster at the high- and low-ionicity ends of the scale, respectively, with the oxyfluorides located between the extremes.

Figure 10(b) also shows that the volume error does not evolve monotonically as a function of *% ionicity* with any of the functionals studied. Although this behavior might arguably reflect the diverse collection of structure types studied, it is significant to note that no clear trends emerge within the hierarchy imposed by Jacob’s ladder of exchange-correlation functionals. Generally, PBEsol shows a remarkable degree of accuracy as a function of *% ionicity*. However, no overall improvement in the accuracy of the cell volume is obtained by using more sophisticated functionals (MS2, SCAN, or HSE06). Furthermore, Fig. 10(b) demonstrates that the evolution of volume as a function of *% ionicity* varies significantly for functionals at the same level of theory, e.g., the metaGGAs MS2 and SCAN.

A semilocal functional can be defined in terms of its enhancement factors  $F_{xc}$  [51], which is typically expressed as a function of the Wigner-Seitz radius,  $r_s = [3/(4\pi n)]^{1/3}$ , the reduced density gradient [44],  $s = |\nabla n|/2(3\pi^2)^{1/3}n^{4/3}$ , and dimensionless parameter  $\alpha$ . The Wigner-Seitz radius is related to the electron density  $n$ , the parameter  $s$  measures how fast the charge density varies on the scale of the local Fermi wavelength  $2\pi/k_F$  where  $k_F = (3\pi^2 n)^{1/3}$  [114,115], and  $\alpha$  is an ingredient of the metaGGAs MS2 and SCAN that characterizes the extent of orbital overlap [43,114].

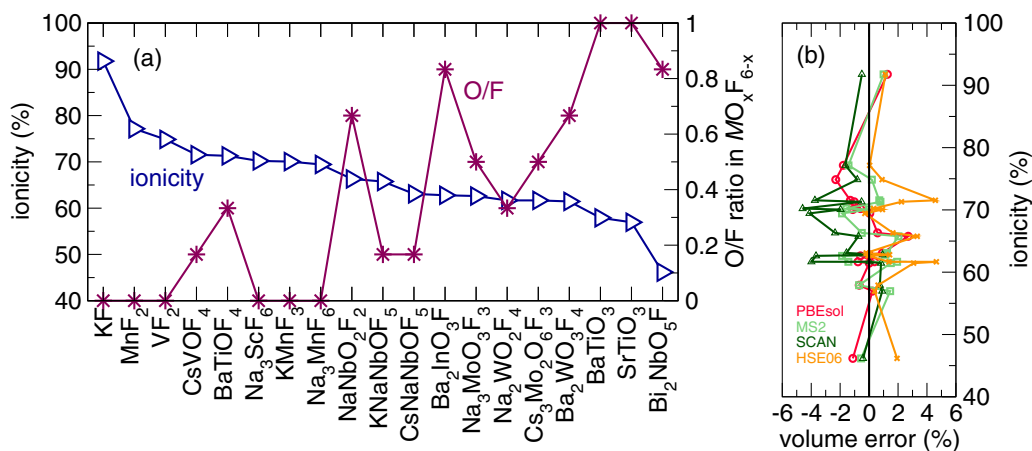


FIG. 10. (a) Calculated ionicities and O/F ratio in the  $MO_xF_{6-x}$  anionic group for the 19 compounds explored. The materials are arranged in order of decreasing ionicity. The electronegativity differences ( $A-B$  interactions) considered in the calculation of the ionicity of the solids were cation-anion and cation-cation. Anion-anion interactions are ignored. (b) Volume error in percentage as a function of ionicity. For clarity, LDA is excluded owing to its large % errors compared to the other functionals.

The spatial distributions of  $r_s$ ,  $s$ , and  $\alpha$  along the [001] direction in the oxyfluoride  $KNaNbOF_5$  ( $x = 1$ ) allow us to identify important regions in the solid [Fig. 11(a)]. [The positions of the ions along the [001] direction are indicated on the upper abscissa of Fig. 11(a).] Specifically, the regions of core-valence separation are characterized by larger values of  $s$  [116], while the regions of single bonding and the overlap of closed shells can be identified where  $\alpha < 1$  and  $\alpha \gg 1$ , respectively [43].

Prior studies have established that a strong correlation exists between predicted cell volumes and the parameters  $r_s$ ,  $s$ , and  $\alpha$  for semilocal functionals [27,51,116,117]. Thus, to better understand the distinct tendencies of the semilocal functionals observed in this work, we plot the exchange ( $E_x$ ) energy density for LDA, PBEsol, MS2, and SCAN [Fig. 11(b)]

[118]. The exchange energy density is  $n(\mathbf{r}) \times E_x(n)$  in LDA or  $n(\mathbf{r}) \times E_x(n) \times F_x(s, \alpha)$  in GGA or metaGGA.  $E_x(n)$  is the exchange energy per particle of LDA, which is a function of  $r_s$ . Interestingly, from the evolution of the  $E_x$  energy density [Fig. 11(b)], we observe that the metaGGA SCAN behaves very similar to LDA, while the other metaGGA MS2 bears closer resemblance to PBEsol. This result is consistent with the trends observed for the functional dependence of the cell volume in the compounds studied, i.e., LDA and SCAN show a strong tendency to underpredict cell volumes, particularly for more ionic compounds, while the absolute errors of the volumes predicted by PBEsol and MS2 are very similar.

Moreover, we observe that the major difference in the  $E_x$  energy density between the LDA and SCAN results and the PBEsol and MS2 results occurs in the region near the core of the ions. It has been shown that for solids, the overlap between the core and the valence electrons of the constituent atoms is a particularly important region for the prediction of the cell volume [27,116]. Indeed, the difference between each semilocal functional is dominated by the analytical form chosen to represent the enhancement factor, but we conjecture that subtle differences in the core-valence regions likely produce the distinct behavior in the structural properties predicted by the functionals with similar  $F_x$  and motivates further detailed analyses.

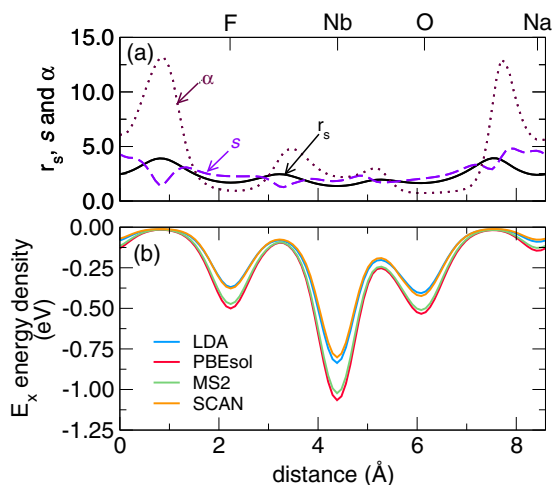


FIG. 11. (a) The computed  $r_s$ ,  $s$ , and  $\alpha$  distributions along a line in the [001] direction within the (100) plane and near the F-Nb-O-Na bond in the compound  $KNaNbOF_5$ . (b) The exchange energy densities along the same path for the functionals LDA, PBEsol, and MS2 and SCAN. The charge density and ELF are computed with PBEsol at the experimental lattice constants.

## V. SUMMARY

We assessed the accuracy of exchange-correlation potentials for DFT found at the first four rungs of Jacob's ladder with an emphasis on predicting the structural, electronic, and lattice dynamical properties in oxyfluorides compounds. The performance of the functionals was found to vary with oxygen content in the octahedral  $MO_xF_{6-x}$  anionic groups. A summary of our main conclusions is as follows:

(a) *Structural properties.* Overall, LDA and PBEsol are consistently the least and most accurate functional for computation of the cell volume and internal coordinates across all materials in our suite, respectively. The modern metaGGAs, MS2 and

SCAN, also show satisfactory performance but do not exhibit the same consistent improvement as the PBEsol functional as the O/F ratio changes. For example, MS2 almost completely removes the tetragonality of BaTiO<sub>3</sub>. It is significant to note that we observe a large variance in the predicted cell volume for the metaGGAs based on the valence configuration of the cation pseudopotentials. We suspect that the discrepancies observed in the structural properties for the metaGGAs may be in part due to the poor transferability of the GGA PAWs used in our study. We suggest a more in-depth pseudopotential study to clarify these observations. The hybrid  $V_{xc}$  HSE06 is indeed most accurate for the fluoride ( $x = 0$ ) and oxide ( $x = 6$ ) compounds; however, it shows a strong tendency to overestimate cell volumes for the oxyfluorides (intermediate integer values of  $x$ ).

(b) *Electronic properties.* All of the compounds in this study are known experimentally to be insulating. Generally, the smallest band gaps are predicted by LDA and PBEsol. The metaGGAs MS2 and SCAN both improve the DFT gap slightly over the functionals at the first two rungs. HSE06 consistently predicts the largest band gaps.

(c) *Lattice dynamical properties.* We computed the phonons for four compounds: KMnF<sub>3</sub> ( $x = 0$ ), KNaNbOF<sub>5</sub> ( $x = 1$ ), Na<sub>2</sub>WO<sub>2</sub>F<sub>4</sub> ( $x = 2$ ), and Na<sub>3</sub>MoO<sub>3</sub>F<sub>3</sub> ( $x = 3$ ). Generally, our results indicate that the phonon frequencies show a strong volume dependence for all XC functionals.

Based on the observations in this study, our general recommendations for DFT calculations of related compounds are as follows: (i) LDA consistently underperforms and, as a result, we do not recommend it for this family of materials; (ii) for all fluoride ( $x = 0$ ) and oxide ( $x = 6$ ) compounds, PBEsol or HSE06 are most accurate; and (iii) for intermediate oxygen compositions ( $x = 1, \dots, 5$ ), PBEsol is consistently accurate for structural properties. In light of this, we also anticipate that functionals which contain *ingredients* based on similar construction principles as PBEsol such as the revised TPSS functional [119] (revTPSS) will yield satisfactory results; however, we advise careful testing of each functional relative to the property being predicted.

#### ACKNOWLEDGMENTS

N.C. and J.M.R. acknowledge support from the National Science Foundation (NSF, Grant No. DMR-1454688) and are grateful to Jianwei Sun for many useful discussions and guidance in using the SCAN functional. N.C. also thanks Liang-Fang Huang and Bing Xiao for useful comments. DFT calculations were performed on the high-performance computing facilities available at the Center for Nanoscale Materials (CARBON Cluster) at Argonne National Laboratory, supported by the U.S. Department of Energy, Office of Basic Energy Sciences (BES), Grant No. DE-AC02-06CH11357.

- 
- [1] J. Tao, J. P. Perdew, V. N. Staroverov, and G. E. Scuseria, Climbing the Density Functional Ladder: Nonempirical Meta-Generalized Gradient Approximation Designed for Molecules and Solids, *Phys. Rev. Lett.* **91**, 146401 (2003).
  - [2] M. Bühl and H. Kabrede, Geometries of transition-metal complexes from density-functional theory, *J. Chem. Theory Comput.* **2**, 1282 (2006).
  - [3] J. Sun, R. C. Remsing, Y. Zhang, Z. Sun, A. Ruzsinszky, H. Peng, Z. Yang, A. Paul, U. Waghmare, X. Wu *et al.*, Accurate first-principles structures and energies of diversely bonded systems from an efficient density functional, *Nat. Chem.* **8**, 831 (2016).
  - [4] D. Rappoport, N. R. M. Crawford, F. Furche, and K. Burke, Approximate density functionals: Which should I choose? in *Encyclopedia of Inorganic Chemistry* (Wiley, New York, 2006).
  - [5] *Anion-Controlled New Inorganic Materials*, edited by I. P. Koutsaroff and A. Fuertes, *Cryst. Growth Des.* **vi**(13) (2014).
  - [6] D. Logvinovich, S. Ebbinghaus, A. Reller, I. Marozau, D. Ferri, and A. Weidenkaff, Synthesis, crystal structure and optical properties of LaNbON<sub>2</sub>, *Z. Anorg. Allg. Chem.* **636**, 905 (2010).
  - [7] M. Yang, J. Orò-Solè, J. A. Rodgers, A. B. Jorge, A. Fuertes, and J. P. Attfield, Anion order in perovskite oxynitrides, *Nat. Chem.* **3**, 47 (2011).
  - [8] A. B. Jorge, J. Orò-Solè, A. M. Bea, N. Mufti, T. T. M. Palstra, J. A. Rodgers, J. P. Attfield, and A. Fuertes, Large coupled magnetoresponses in EuNbO<sub>2</sub>N, *J. Am. Chem. Soc.* **130**, 12572 (2008).
  - [9] D. C. Johnston, The puzzle of high temperature superconductivity in layered iron pnictides and chalcogenides, *Adv. Phys.* **59**, 803 (2010).
  - [10] *Photonic and Electronic Properties of Fluoride Materials*, edited by A. Tressaud and K. Poeppelmeier (Elsevier, Boston, 2016).
  - [11] V. L. Chevrier, G. Hautier, S. P. Ong, R. E. Doe, and G. Ceder, First-principles study of iron oxyfluorides and lithiation of FeOF, *Phys. Rev. B* **87**, 094118 (2013).
  - [12] J. T. Inconvati, L. F. Wan, B. Key, D. Zhou, C. Liao, L. Fuoco, M. Holland, H. Wang, D. Prendergast, K. R. Poeppelmeier, and J. T. Vaughey, Reversible magnesium intercalation into a layered oxyfluoride cathode, *Chem. Mater.* **28**, 17 (2016).
  - [13] A. A. Setlur, E. V. Radkov, C. S. Henderson, J.-H. Her, A. M. Srivastava, N. Karkada, M. S. Kishore, N. P. Kumar, D. Aesram, A. Deshpande, B. Kolodin, L. S. Grigorov, and U. Happek, Energy-efficient, high-color-rendering LED lamps using oxyfluoride and fluoride phosphors, *Chem. Mater.* **22**, 4076 (2010).
  - [14] W. B. Im, S. Brinkley, J. Hu, A. Mikhailovsky, S. P. DenBaars, and R. Seshadri, Sr<sub>2.975-x</sub>Ba<sub>x</sub>Ce<sub>0.025</sub>AlO<sub>4</sub>F: A highly efficient green-emitting oxyfluoride phosphor for solid state white lighting, *Chem. Mater.* **22**, 2842 (2010).
  - [15] V. V. Atuchin, L. I. Isaenko, V. G. Kesler, Z. S. Lin, M. S. Molokeev, A. P. Yeliseyev, and S. A. Zhurkov, Exploration on anion ordering, optical properties and electronic structure in K<sub>3</sub>WO<sub>3</sub>F<sub>3</sub> elpasolite, *J. Solid State Chem.* **187**, 159 (2012).

- [16] H. K. Izumi, J. E. Kirsch, C. L. Stern, and K. R. Poeppelmeier, Examining the out-of-center distortion in the  $[\text{NbOF}_5]^{2-}$  anion, *Inorg. Chem.* **44**, 884 (2005).
- [17] C. de la Cruz, Q. Huang, J. W. Lynn, J. Li, W. Ratcliff II, J. L. Zarestky, H. A. Mook, G. F. Chen, J. L. Luo, N. L. Wang, and P. Dai, Magnetic order close to superconductivity in the iron-based layered  $\text{LaO}_{1-x}\text{F}_x\text{FeAs}$  systems, *Nature (London)* **453**, 899 (2008).
- [18] Y. Kamihara, T. Watanabe, M. Hirano, and H. Hosono, Iron-based layered superconductor  $\text{LaO}_{[1-x}\text{F}_x]\text{FeAs}$  ( $x = 0.05 - 0.12$ ) with  $T_c = 26$  K, *J. Am. Chem. Soc.* **130**, 3296 (2008).
- [19] R. D. Shannon and C. T. Prewitt, Revised values of effective ionic radii, *Acta Crystallogr. Sect. B* **26**, 1046 (1970).
- [20] R. L. Withers, F. J. Brink, Y. Liu, and L. Norén, Cluster chemistry in the solid state: Structured diffuse scattering, oxide/fluoride ordering and polar behavior in transition metal oxyfluorides, *Polyhedron* **26**, 290 (2007).
- [21] G. Kresse and J. Furthmüller, Efficient iterative schemes for *ab initio* total-energy calculations using a plane-wave basis set, *Phys. Rev. B* **54**, 11169 (1996).
- [22] G. Kresse and D. Joubert, From ultrasoft pseudopotentials to the projector augmented-wave method, *Phys. Rev. B* **59**, 1758 (1999).
- [23] P. E. Blöchl, Projector augmented-wave method, *Phys. Rev. B* **50**, 17953 (1994).
- [24] See Supplemental Material at <http://link.aps.org/supplemental/10.1103/PhysRevB.94.174108> for additional computational details, crystal structure information, and GII calculations.
- [25] H. J. Monkhorst and J. D. Pack, Special points for Brillouin-zone integrations, *Phys. Rev. B* **13**, 5188 (1976).
- [26] A. Togo, F. Oba, and I. Tanaka, First-principles calculations of the ferroelastic transition between rutile-type and  $\text{CaCl}_2$ -type  $\text{SiO}_2$  at high pressures, *Phys. Rev. B* **78**, 134106 (2008).
- [27] M. Fuchs, M. Bockstedte, E. Pehlke, and M. Scheffler, Pseudopotential study of binding properties of solids within generalized gradient approximations: The role of core-valence exchange correlation, *Phys. Rev. B* **57**, 2134 (1998).
- [28] J. P. Perdew and K. Schmidt, Jacob's ladder of density functional approximations for the exchange-correlation energy, *AIP Conf. Proc.* **577**, 1 (2001).
- [29] W. Kohn and L. J. Sham, Self-consistent equations including exchange and correlation effects, *Phys. Rev.* **140**, A1133 (1965).
- [30] R. Wahl, D. Vogtenhuber, and G. Kresse,  $\text{SrTiO}_3$  and  $\text{BaTiO}_3$  revisited using the projector augmented wave method: Performance of hybrid and semilocal functionals, *Phys. Rev. B* **78**, 104116 (2008).
- [31] J. P. Perdew and Y. Wang, Accurate and simple density functional for the electronic exchange energy: Generalized gradient approximation, *Phys. Rev. B* **33**, 8800(R) (1986).
- [32] A. D. Becke, Density functional thermochemistry. I. The effect of the exchange only gradient correction, *J. Chem. Phys.* **96**, 2155 (1992).
- [33] J. P. Perdew, J. A. Chevary, S. H. Vosko, K. A. Jackson, M. R. Pederson, D. J. Singh, and C. Fiolhais, Atoms, molecules, solids, and surfaces: Applications of the generalized gradient approximation for exchange and correlation, *Phys. Rev. B* **46**, 6671 (1992).
- [34] J. P. Perdew, K. Burke, and M. Ernzerhof, Generalized Gradient Approximation made Simple, *Phys. Rev. Lett.* **77**, 3865 (1996).
- [35] K. Burke, Perspective on density functional theory, *J. Chem. Phys.* **136**, 150901 (2012).
- [36] J. P. Perdew, A. Ruzsinszky, G. I. Csonka, O. A. Vydrov, G. E. Scuseria, L. A. Constantin, X. Zhou, and K. Burke, Restoring the Density-Gradient Expansion for Exchange in Solids and Surfaces, *Phys. Rev. Lett.* **100**, 136406 (2008).
- [37] Z. Wu and R. E. Cohen, More accurate generalized gradient approximation for solids, *Phys. Rev. B* **73**, 235116 (2006).
- [38] L. A. Constantin, A. Terentjev, F. D. Sala, P. Cortona, and E. Fabiano, Semiclassical atom theory applied to solid-state physics, *Phys. Rev. B* **93**, 045126 (2016).
- [39] V. N. Staroverov, G. E. Scuseria, J. Tao, and J. P. Perdew, Tests of a ladder of density functionals for bulk solids and surfaces, *Phys. Rev. B* **69**, 075102 (2004).
- [40] J. Sun, A. Ruzsinszky, and J. P. Perdew, Strongly Constrained and Appropriately Normed Semilocal Density Functional, *Phys. Rev. Lett.* **115**, 036402 (2015).
- [41] P. Haas, F. Tran, and P. Blaha, Calculation of the lattice constant of solids with semilocal functionals, *Phys. Rev. B* **79**, 085104 (2009).
- [42] J. Sun, B. Xiao, and A. Ruzsinszky, Communication: Effect of the orbital-overlap dependence in the meta-generalized gradient approximation, *J. Chem. Phys.* **137**, 051101 (2012).
- [43] J. Sun, B. Xiao, Y. Fang, R. Haunschild, P. Hao, A. Ruzsinszky, G. I. Csonka, G. E. Scuseria, and J. P. Perdew, Density Functionals that Recognize Covalent, Metallic, and Weak Bonds, *Phys. Rev. Lett.* **111**, 106401 (2013).
- [44] J. Sun, R. Haunschild, B. Xiao, I. W. Bulik, G. E. Scuseria, and J. P. Perdew, Semilocal and hybrid meta-generalized gradient approximations based on the understanding of the kinetic-energy-density dependence, *J. Chem. Phys.* **138**, 044113 (2013).
- [45] B. Silvi, A. Savin *et al.*, Classification of chemical bonds based on topological analysis of electron localization functions, *Nature (London)* **371**, 683 (1994).
- [46] A. D. Becke and K. E. Edgecombe, A simple measure of electron localization in atomic and molecular systems, *J. Chem. Phys.* **92**, 5397 (1990).
- [47] F. D. Sala, E. Fabiano, and L. A. Constantin, Kohn-Sham kinetic energy density in the nuclear and asymptotic regions: Deviations from the von Weizsäcker behavior and applications to density functionals, *Phys. Rev. B* **91**, 035126 (2015).
- [48] L. A. Constantin, E. Fabiano, J. M. Pitarke, and F. D. Sala, Semilocal density functional theory with correct surface asymptotics, *Phys. Rev. B* **93**, 115127 (2016).
- [49] Y. Zhao and D. G. Truhlar, A new local density functional for main-group thermochemistry, transition metal bonding, thermochemical kinetics, and noncovalent interactions, *J. Chem. Phys.* **125**, 194101 (2006).
- [50] J. Tao and Y. Mo, Accurate Semilocal Density Functional for Condensed-Matter Physics and Quantum Chemistry, *Phys. Rev. Lett.* **117**, 073001 (2016).
- [51] F. Tran, J. Stelzl, and P. Blaha, Rungs 1 to 4 of DFT Jacob's ladder: Extensive test on the lattice constant, bulk modulus, and cohesive energy of solids, *J. Chem. Phys.* **144**, 204120 (2016).
- [52] A. D. Becke, Density-functional thermochemistry. III. The role of exact exchange, *J. Chem. Phys.* **98**, 5648 (1993).
- [53] T. Archer, C. D. Pemmaraju, S. Sanvito, C. Franchini, J. He, A. Filippetti, P. Delugas, D. Puggioni, V. Fiorentini, R. Tiwari,

- and P. Majumdar, Exchange interactions and magnetic phases of transition metal oxides: Benchmarking advanced *ab initio* methods, *Phys. Rev. B* **84**, 115114 (2011).
- [54] J. P. Perdew, M. Ernzerhof, and K. Burke, Rationale for mixing exact exchange with density functional approximations, *J. Chem. Phys.* **105**, 9982 (1996).
- [55] J. Heyd, J. E. Peralta, G. E. Scuseria, and R. L. Martin, Energy band gaps and lattice parameters evaluated with the Heyd-Scuseria-Ernzerhof screened hybrid functional, *J. Chem. Phys.* **123**, 174101 (2005).
- [56] M. A. L. Marques, J. Vidal, M. J. T. Oliveira, L. Reining, and S. Botti, Density-based mixing parameter for hybrid functionals, *Phys. Rev. B* **83**, 035119 (2011).
- [57] P. Garcia-Fernandez, S. Ghosh, N. J. English, and J. A. Aramburu, Benchmark study for the application of density functional theory to the prediction of octahedral tilting in perovskites, *Phys. Rev. B* **86**, 144107 (2012).
- [58] J. He and C. Franchini, Screened hybrid functional applied to  $3d^0 \rightarrow 3d^8$  transition-metal perovskites  $\text{LaMO}_3$  ( $M = \text{Sc} - \text{Cu}$ ): Influence of the exchange mixing parameter on the structural, electronic, and magnetic properties, *Phys. Rev. B* **86**, 235117 (2012).
- [59] G. I. Finch and S. Fordham, The effect of crystal-size on lattice-dimensions, *Proc. Phys. Soc.* **48**, 85 (1936).
- [60] M. M. R. Costa and M. J. M. de Almeida, Asphericity effects in the electron density of  $\text{VF}_2$ , *Acta Crystallogr. Sect. B* **43**, 346 (1987).
- [61] W. H. Baur and A. A. Khan, Rutile-type compounds. IV.  $\text{SiO}_2$ ,  $\text{GeO}_2$  and a comparison with other rutile-type structures, *Acta Cryst. B* **27**, 2133 (1971).
- [62] V. Scatturin, L. Corliss, N. Elliott, and J. Hastings, Magnetic structures of  $3d$  transition metal double fluorides,  $\text{KMeF}_3$ , *Acta Crystallogr.* **14**, 19 (1961).
- [63] S. Carlson, Y. Xu, and R. Norrestam, Single-crystal high-pressure studies of  $\text{Na}_3\text{ScF}_6$ , *J. Solid State Chem.* **135**, 116 (1998).
- [64] S. Carlson, Y. Xu, U. Hålenius, and R. Norrestam, A reversible, isosymmetric, high-pressure phase transition in  $\text{Na}_3\text{MnF}_6$ , *Inorg. Chem.* **37**, 1486 (1998).
- [65] F. C. Hawthorne and R. B. Ferguson, Refinement of the crystal structure of cryolite, *Can. Mineralog.* **13**, 377 (1975).
- [66] R. A. F. Pinlac, C. L. Stern, and K. R. Poeppelmeier, New Layered Oxide-Fluoride Perovskites:  $\text{KNaNbOF}_5$  and  $\text{KNaMO}_2\text{F}_4$  ( $M = \text{Mo}^{6+}, \text{W}^{6+}$ ), *Crystals* **1**, 3 (2011).
- [67] G. W. Bushnell and K. C. Moss, The crystal structure of caesium oxotetrafluorovanadate (V), *Can. J. Chem.* **50**, 3700 (1972).
- [68] M. R. Marvel, J. Lesage, J. Baek, P. S. Halasyamani, C. L. Stern, and K. R. Poeppelmeier, Cation-anion interactions and polar structures in the solid state, *J. Am. Chem. Soc.* **129**, 13963 (2007).
- [69] M. Vlasse, J. M. Moutou, M. Cervera-Marzal, J.-P. Chaminade, and P. Hagenmüller, Structure of  $\text{Na}_2\text{WO}_2\text{F}_4$ , *Rev. Chim. Miner.* **19**, 58 (1982).
- [70] M. P. Crosnier and J. L. Fourquet, Synthesis and crystal structure of  $\text{BaTiOF}_4$ , *Eur. J. Solid State Inorg. Chem.* **29**, 199 (1992).
- [71] F. J. Brink, L. Norén, D. J. Goossens, R. L. Withers, Y. Liu, and C.-N. Xu, A combined diffraction (XRD, electron and neutron) and electrical study of  $\text{Na}_3\text{MoO}_3\text{F}_3$ , *J. Solid State Chem.* **174**, 450 (2003).
- [72] R. Mattes, K. Mennemann, N. Jäckel, H. Rieskamp, and H.-J. Brockmeyer, Structure and properties of the fluorine-rich oxofluoromolybdates  $\text{Cs}_3[\text{Mo}_2\text{O}_6\text{F}_3]$ ,  $(\text{NH}_4)_3[\text{Mo}_2\text{O}_2\text{F}_9]$  and  $(\text{NH}_4)_2[\text{MoOF}_5]$ , *J. Less-Common Met.* **76**, 199 (1980).
- [73] C. C. Torardi and L. H. Brixner, Structure and luminescence of  $\text{Ba}_2\text{WO}_3\text{F}_4$ , *Mater. Res. Bull.* **20**, 137 (1985).
- [74] E. E. McCabe, I. P. Jones, D. Zhang, N. C. Hyatt, and C. Greaves, Crystal structure and electrical characterisation of  $\text{Bi}_2\text{NbO}_5\text{F}$ : An Aurivillius oxide fluoride, *J. Mater. Chem.* **17**, 1193 (2007).
- [75] R. L. Needs and M. T. Weller, Synthesis and structure of  $\text{Ba}_2\text{InO}_3\text{F}$ : Oxide/fluoride ordering in a new  $\text{K}_2\text{NiF}_4$  superstructure, *J. Chem. Soc., Chem. Commun.*, 353 (1995).
- [76] J. M. Kiat and T. Roisnel, Rietveld analysis of strontium titanate in the müller state, *J. Phys.: Condens. Matter* **8**, 3471 (1996).
- [77] R. H. Buttner and E. N. Maslen, Structural parameters and electron difference density in  $\text{BaTiO}_3$ , *Acta Crystallogr. Sect. B* **48**, 764 (1992).
- [78] A. Tressaud and J.-M. Dance, Relationships between structure and low-dimensional magnetism in fluorides, in *Structures versus Special Properties*, edited by D. Reinen (Springer, Berlin, Heidelberg, 1982), p. 87.
- [79] J. C. Slater, Magnetic effects and the Hartree-Fock equation, *Phys. Rev.* **82**, 538 (1951).
- [80] K. Saiki, Resonance behavior in canted antiferromagnet  $\text{KMnF}_3$ , *J. Phys. Soc. Jpn.* **33**, 1284 (1972).
- [81] N. Charles and J. M. Rondinelli, Microscopic origin of pressure-induced isosymmetric transitions in fluoromanganate cryolites, *Phys. Rev. B* **90**, 094114 (2014).
- [82] M. T. Czyżyk and G. A. Sawatzky, Local-density functional and on-site correlations: The electronic structure of  $\text{La}_2\text{CuO}_4$  and  $\text{LaCuO}_3$ , *Phys. Rev. B* **49**, 14211 (1994).
- [83] A. I. Liechtenstein, V. I. Anisimov, and J. Zaanen, Density-functional theory and strong interactions: Orbital ordering in mott-hubbard insulators, *Phys. Rev. B* **52**, R5467 (1995).
- [84] Y. He, Heat capacity, thermal conductivity, and thermal expansion of barium titanate-based ceramics, *Thermochim. Acta* **419**, 135 (2004).
- [85] L.-F. Huang, X.-Z. Lu, E. Tennesen, and J. M. Rondinelli, An efficient ab-initio quasiharmonic approach for the thermodynamics of solids, *Comput. Mater. Sci.* **120**, 84 (2016).
- [86] G. de la Flor, D. Orobengoa, E. Tasci, J. M. Perez-Mato, and M. I. Aroyo, Comparison of structures applying the tools available at the Bilbao Crystallographic Server, *J. Appl. Crystallogr.* **49**, 653 (2016).
- [87] I. D. Brown and K. R. Poeppelmeier, *Bond Valences*, Vol. 158 (Springer-Verlag, Berlin, Heidelberg, 2014).
- [88] S. Adams, O. Moretzki, and E. Canadell, Global instability index optimizations for the localization of mobile protons, *Solid State Ionics* **168**, 281 (2004).
- [89] P. Garcia-Fernandez, J. A. Aramburu, M. T. Barriuso, and M. Moreno, Key role of covalent bonding in octahedral tilting in perovskites, *J. Phys. Chem. Lett.* **1**, 647 (2010).
- [90] G. Shirane, H. Danner, and R. Pepinsky, Neutron diffraction study of orthorhombic  $\text{BaTiO}_3$ , *Phys. Rev.* **105**, 856 (1957).

- [91] D. I. Bilc, R. Orlando, R. Shaltaf, G.-M. Rignanese, Jorge Íñiguez, and Ph. Ghosez, Hybrid exchange-correlation functional for accurate prediction of the electronic and structural properties of ferroelectric oxides, *Phys. Rev. B* **77**, 165107 (2008).
- [92] Z. Wu, R. E. Cohen, and D. J. Singh, Comparing the weighted density approximation with the LDA and GGA for ground-state properties of ferroelectric perovskites, *Phys. Rev. B* **70**, 104112 (2004).
- [93] A. M. Fox, *Optical Properties of Solids*, Vol. 3 (Oxford University Press, New York, 2001).
- [94] K. van Benthem, C. Elsässer, and R. H. French, Bulk electronic structure of SrTiO<sub>3</sub>: Experiment and theory, *J. Appl. Phys.* **90**, 6156 (2001).
- [95] S. H. Wemple, Polarization fluctuations and the optical-absorption edge in BaTiO<sub>3</sub>, *Phys. Rev. B* **2**, 2679 (1970).
- [96] Z. Yang, H. Peng, J. Sun, and J. P. Perdew, More realistic band gaps from meta-generalized gradient approximations: Only in a generalized Kohn-Sham scheme, *Phys. Rev. B* **93**, 205205 (2016).
- [97] J. Kapusta, P. Daniel, and A. Ratuszna, Revised structural phase transitions in the archetype KMnF<sub>3</sub> perovskite crystal, *Phys. Rev. B* **59**, 14235 (1999).
- [98] M. A. Islam, J. M. Rondinelli, and J. E. Spanier, Normal mode determination of perovskite crystal structures with octahedral rotations: Theory and applications, *J. Phys.: Condens. Matter* **25**, 175902 (2013).
- [99] J. D. Axe and G. D. Pettit, Infrared dielectric dispersion of several fluoride perovskites, *Phys. Rev.* **157**, 435 (1967).
- [100] A. S. Krylov, S. N. Sofronova, E. M. Kolesnikova, Yu. N. Ivanov, A. A. Sukhovskiy, S. V. Goryainov, A. A. Ivanenko, N. P. Shestakov, A. G. Kocharova, and A. N. Vtyurin, Experimental and theoretical methods to study structural phase transition mechanisms in K<sub>3</sub>WO<sub>3</sub>F<sub>3</sub> oxyfluoride, *J. Solid State Chem.* **218**, 32 (2014).
- [101] E. I. Voit, A. V. Voit, A. A. Mashkovskii, N. M. Laptash, and V. Ya. Kavun, Dynamic disorder in ammonium oxofluorination states (NH<sub>4</sub>)<sub>2</sub>WO<sub>2</sub>F<sub>4</sub> and (NH<sub>4</sub>)<sub>3</sub>WO<sub>3</sub>F<sub>3</sub>, *J. Struct. Chem.* **47**, 642 (2006).
- [102] O. L. Keller Jr., Identification of complex ions of niobium(V) in hydrofluoric acid solutions by raman and infrared spectroscopy, *Inorg. Chem.* **2**, 783 (1963).
- [103] G. Pausewang and W. Rüdorff, Über alkali-oxofluorometallate der Übergangsmetalle. A<sub>3</sub>MeO<sub>x</sub>F<sub>6-x</sub>-verbindungen mit x = 1, 2, 3, *Z. Anorg. Allg. Chem.* **364**, 69 (1969).
- [104] A. S. Krylov, E. M. Merkusheva, A. N. Vtyurin, and L. I. Isaenko, Raman spectroscopic study of the lattice dynamics in the Rb<sub>2</sub>KMoO<sub>3</sub>F<sub>3</sub> oxyfluoride, *Phys. Solid State* **54**, 1275 (2012).
- [105] K. Dehnicke, G. Pausewang, and W. Rüdorff, Die ir-spektren der oxofluorokomplexe TiOF<sub>5</sub><sup>3-</sup>, VOF<sub>5</sub><sup>3-</sup>, NbO<sub>2</sub>F<sub>4</sub><sup>3-</sup>, MoO<sub>3</sub>F<sub>3</sub><sup>3-</sup> und WO<sub>3</sub>F<sub>3</sub><sup>3-</sup>, *Z. Anorg. Allg. Chem.* **366**, 64 (1969).
- [106] C. R. A. Catlow and A. M. Stoneham, Ionicity in solids, *J. Phys. C* **16**, 4321 (1983).
- [107] J. A. Duffy, Chemical bonding in the oxides of the elements: A new appraisal, *J. Solid State Chem.* **62**, 145 (1986).
- [108] J. Meister and W. H. E. Schwarz, Principal components of ionicity, *J. Phys. Chem.* **98**, 8245 (1994).
- [109] A. Cammarata and J. M. Rondinelli, Covalent dependence of octahedral rotations in orthorhombic perovskite oxides, *J. Chem. Phys.* **141**, 114704 (2014).
- [110] R. E. Cohen, Origin of ferroelectricity in perovskite oxides, *Nature (London)* **358**, 136 (1992).
- [111] J. A. Van Vechten, Quantum dielectric theory of electronegativity in covalent systems. I. Electronic dielectric constant, *Phys. Rev.* **182**, 891 (1969).
- [112] A. Whiteside, S. S. Xantheas, and M. Gutowski, Is electronegativity a useful descriptor for the pseudo-alkali metal NH<sub>4</sub>? *Chem. Eur. J.* **17**, 13197 (2011).
- [113] L. Pauling, The nature of the chemical bond. IV. The energy of single bonds and the relative electronegativity of atoms, *J. Am. Chem. Soc.* **54**, 3570 (1932).
- [114] B. Xiao, J. Sun, A. Ruzsinszky, J. Feng, R. Haunschild, G. E. Scuseria, and J. P. Perdew, Testing density functionals for structural phase transitions of solids under pressure: Si, SiO<sub>2</sub>, and Zr, *Phys. Rev. B* **88**, 184103 (2013).
- [115] J. P. Perdew, K. Burke, and Y. Wang, Generalized gradient approximation for the exchange-correlation hole of a many-electron system, *Phys. Rev. B* **54**, 16533 (1996).
- [116] P. Haas, F. Tran, P. Blaha, K. Schwarz, and R. Laskowski, Insight into the performance of GGA functionals for solid-state calculations, *Phys. Rev. B* **80**, 195109 (2009).
- [117] G. I. Csonka, J. P. Perdew, A. Ruzsinszky, P. H. T. Philipsen, S. Lebègue, J. Paier, O. A. Vydrov, and J. G. Ángyán, Assessing the performance of recent density functionals for bulk solids, *Phys. Rev. B* **79**, 155107 (2009).
- [118] The exchange energy density is  $n(\mathbf{r}) \times E_x(n)$  in LDA or  $n(\mathbf{r}) \times E_x(n) \times F_x(s, \alpha)$  in GGA or metaGGA.  $E_x(n)$  is the exchange energy per particle of LDA, which is a function of  $r_s$ .
- [119] J. P. Perdew, A. Ruzsinszky, G. I. Csonka, L. A. Constantin, and J. Sun, Workhorse Semilocal Density Functional for Condensed Matter Physics and Quantum Chemistry, *Phys. Rev. Lett.* **103**, 026403 (2009).